Chapter 4

Zinc Oxide Thin Films: Nano-structures Formation, Properties and Gas Sensors Application

Controlled growth of zinc oxide (ZnO) nano-structures, starting from a vertical nano-wall surface morphology to a laterally grown nano-rods/wires formation is studied here by systematically controlling the surface kinetics and thermodynamics. Thin Zn films of variable thickness (~100 nm) were deposited on glass and silicon substrates using a vacuum assisted thermal evaporation technique followed by thermal oxidation in air ambient at different temperatures from RT to 1000°C. Different analytical properties of ZnO films such as electrical, structural, morphological, chemical and optical properties were investigated using various surface characterization techniques such as four probe measurement techniques, X-ray diffraction (XRD), scanning electron microscopy (SEM), tunneling electron microscopy (TEM), X-ray photoemission spectroscopy (XPS) and Raman spectroscopy.

XRD results in association with SEM findings show nice vertical growth morphology of ZnO nano-wall/sheet structures at relatively lower oxidation temperature below 450°C. However, the transition from vertical to lateral growth morphology of two dimensional (2D) layered growths is observed for oxidation of Zn films at about 450 °C. At even higher oxidation temperature of about 650 °C promotes an anisotropic lateral growth. Formation of one dimensional (1D) ZnO nanostructures starts to dominate over the vertical growth. Oxidation of Zn films at 700 °C results in asymmetric growth front and appears with laterally grown 1D ZnO nano-wires/rods of high density. Raman spectroscopy and XPS results suggest that, within the kinetic limitation, vertical growth is mainly controlled by the initial metallic Zn film surface morphology. However, the lateral growth of ZnO layered structures is strongly dominated by the oxide formation. TEM results are complementary with the SEM findings and suggest the 1D growth of ZnO nano-rods are mostly driven by the reduced surface free energy at thermodynamic equilibrium.

Similar to earlier gas sensing studies, these ZnO based nano-structured (nano-rods and nano-porous) thin films are used for CO gas and ethanol vapors sensing and their sensing abilities are compared. In contrast to CuO thin film based CO sensors, ZnO nanostructures grown at relatively higher oxidation temperature exhibit a superior response to CO gas as compared to that grown at lower oxidation temperature. ZnO thin films with nano-rods surface morphology (oxidation at 700°C) shows a strong CO response within an operating temperature ranging from 150 to 270°C. A significantly high CO response of about 19% is obtained at an operating temperature of 200°C and a CO concentration of 220 ppm. In addition, these ZnO nano-rods are also able to sense the ethanol vapour at room temperature. Overall, ZnO nano-rods possess multifunctional properties and have the potential in CO gas and ethanol vapor detection at different operating temperatures.

4.1   INTRODUCTION

In general, ZnO is an n-type semiconductor with a direct band gap of about 3.3–3.5 eV [1] and exhibits a wurtzite crystal structure [2]. One of the most exciting features of ZnO film is that it may appear in a variety of nano-structured surface morphologies staring from zero dimensional (0D) nano-particles; 1D nano-rods [3], needles [4], and wires [5]; 2D nano-sheets [6], thin films and pellets; and 3D nano-flowers [7]. Different researches have successfully grown low dimensional ZnO nanostructures using both physical as well as chemical routes. ZnO based nanostructures are largely classified with their potential applications in the fields of sensor and device applications. Several reports on formation of ZnO based nanostructures are widely available. However the growth mechanism behind the nano-structure formation is still very much limited. Therefore, self organized growth mechanisms of different ZnO nano-materials having significantly different structure, morphology and stoichiometry are of high technological demand.

In principle MOS based resistive mode gas sensing mechanism always demands a very high surface to volume ratio of the active materials. As ZnO appears in a variety of nanostructures, it appears to be a potential candidate for gas sensor material. In recent days, ZnO based nano-structures are one of the most widely used materials in the field of gas sensor applications. Unintentional O_2 vacancy in ZnO usually leads to a stoichiometry issues, which in principle limits/controls its gas sensing (electronic) performance. In addition, the surface redox chemistry, during its exposure to any gas or vapour molecules, plays a very crucial role on the gas sensing mechanism. More details about zinc oxides (ZnO) and its applications are already discussed in Chapter 1.

ZnO nanostructured based various gas sensors for dangerous and poisonous gases like NH_3 [8], NO_2 [9], H_2 [10], CO [11], CO_2 [12], ethanol [13] and LPG [14] have already been reported. In order to improve the gas sensing ability of ZnO based sensors, several approached have been explored. Recently, 1D ZnO nanostructures based gas sensors have been fabricated with an enhanced sensitivity [15]. However, most of the ZnO nano-wires appear without any alignment symmetry [16-17]. Various metals / (nano-particles) have also been doped / (decorated) in / (on) ZnO thin films to improve the selectivity. As an example Au doped ZnO can detect NO_2 [18] efficiently while Sn doped ZnO shows good sensitivity to ethanol vapor [19]. On the other hand the Pd particles are used as a application of H_2 strogaes (maximum H_2 storage 0.38 wt.%),

which was successfully deposited on the surface of disordered mesoporous carbon spheres (DMHCS) [20]. Whereas, explore of super active and durable bi-functional electro catalyst is a great challenge for researches, which can be achieved using copper (Cu) and cobalt (Co) nano-particle co-decorated N-doped graphene nano-sheets. In this case the co-decoration of copper and cobalt nano-particles due to the strong electron transfer between Cu and Co, enhanced active surface area and strongly facilitated reaction kinetics [21].

Apart from the gas sensing properties, wide band gap of ZnO makes it useful for optoelectronic device applications such as blue light emitting diodes (LED) [22], UV laser [23], and UV detector [24-25] etc. ZnO thin films are also transparent to the visible light which makes it useful for solar cell application as a transparent conducting electrode in flat panel display and window layer for visible lights [26-28]. Piezo and pyroelectric behaviors are the unique property of ZnO based m-aterials. Due to its piezoelectric properties and bio-degradability, it is capable to be utilized in the ceramics industry as well as in field of biomedicine [29]. In addition, it is having excellent mechanical and thermal stability at room temperature [30].

In this chapter, a controlled oxidation of thin Zn films leading towards the formation of ZnO nanostructures, starting from a 2D vertical nano-wall surface morphology to laterally grown nano-rods/wires, is presented by systematically varying the oxidation temperature of the thin Zn films. Afterwards, these ZnO nanostructures are successfully used for CO gas and ethanol vapour sensing at relatively lower operating temperature. Nano-rods surface morphology is having an advantage of high surface area over other nanostructures and appears to be superior for CO sensing. In any case, surface electronic properties of the ZnO films are strongly influenced by surface oxidation process where ZnO nano-rods are found to be highly sensitive for CO and ethanol sensing. The growth mechanism of various ZnO nano-structures is found to be mostly controlled by the thermal diffusion and modulation of the surface free energy. All ZnO based nanostructures are analytically characterized and their corresponding material properties are discussed with a special focus towards the gas sensing application. Two different gas sensing applications of these ZnO based nanostructures such as reducing gas carbon monoxide (CO) and oxidizing vapour ethanol (C_2H_5OH) are briefly discussed in the following.

CO sensing: Among different gases, carbon monoxide (CO) is getting a particular attention because of its colorless, odorless and tasteless nature. The sensing of CO gas through human body is very difficult and it can easily slow up the blood's ability to carry oxygen. CO gas can easily displace the oxygen within the blood and dispossess to the heart, brain and other vital organs. Large amounts of CO inhalation can cause suffocation, unconsciousness, headache, fatigue, dizziness, drowsiness, nausea or even death. Therefore, early detection of any CO poisoning for even of very low concentration is highly desirable. Moreover, a comparison between the p-type CuO and the n-type ZnO nanostructures for CO sensing are also of high scientific interest.

Ethanol sensing: In addition to CO sensing, ethanol vapour sensing is also very important because of it's incredibly versatile property. Ethanol can easily be mixed with water, chlorides and hydrocarbons and some other solvents. The effects of ethanol on human health can vary in a wide range such as nausea, vomiting, dizziness etc. Excessive use of alcoholic beverages for long term may cause even respiratory paralysis, liver cirrhosis, cancers and nervous system disorders. At the same time, ethanol vapor have a great importance in the applications of hygiene products, bio-fuel, gasoline, medicines as well as the preservation of biochemical samples. Moreover, it can very much be useful for sanitization against different microbes such as corona viruses.

4.2   EXPERIMENTAL DETAILS

Thin Zn films were deposited on glass and silicon substrates at room temperature using a vacuum assisted thermal evaporation technique. Prior to any deposition, substrates were ultrasonically cleaned using ethanol, acetone and iso-propanol in *ex-situ* and then dried under dry N_2 gas. During the Zn deposition, vacuum chamber pressure remained $\sim 10^{-5}$ mbar and the evaporation rate was maintained about ~ 3 Å/sec to have a uniform and homogeneous Zn film surface. Afterwards, as-grown Zn films were thermally oxidized within a furnace in air ambient at different oxidation temperatures starting from RT to 1000°C. All oxidations were carried out for sufficiently long duration, even up to 10hr, to assure the thermodynamic equilibrium of the oxide films. A slow cooling rate (10°C/ min) was preferred to minimize the possible thermal stress and improve crystalline quality of the films.

Afterwards, ZnO films were characterized for structural, morphological, electrical, chemical and optical properties using various analytical techniques. To investigate the initial oxidation of Zn thin films, sheet resistance of the Zn thin films was measured by the four point probes technique with a probe-spacing of *2 mm*, using the Physical Quantity Measurement System (PQMS) from Qazartech. The crystallographic structures of the oxide films were investigated by Rigaku Mini Flux II X-ray diffractometer (XRD) with *Cu-Kα* radiation $(\lambda = 1.54\ \AA)$. In addition, transmission electron microscopy (TEM) was also used to investigate the texture and crystal orientation of the ZnO nanostructures. Surface morphology of the copper oxide films was analyzed with a commercial field emission scanning electron microscopy (FESEM). Raman spectroscopy measurements were also performed to distinguish the oxide phases of the films, using a commercial Raman spectrometer from Horiba Scientific. Finally, X-ray photoelectron spectroscopy (XPS) measurement was performed to find the oxidation states of Zn and the purity of the oxides layer. During XPS measurements, the base pressure of the chamber was maintained below $< 10^{-9}$ mBar and monochromatic Al K_{α} (1486.6 eV) and *Mg K_{α}* (*1256.7 eV*) lines were used as X-ray sources. All binding energies of the emitted photoelectrons are calibrated to the C1s line at 284.5 eV.

4.3   RESULTS AND DISCUSSION

Control growth of ZnO based nanostructures by modulating the surface kinetic and thermodynamics as well as their various analytical characterizations are presented here. In addition, a possible growth mechanism for ZnO nanostructure growth has also been discussed within this section.

4.3.1 Thermal oxidation process of thin zinc films

Effect of oxidation temperatures and durations on the oxidation process of thin Zn films, leading towards the formation of different ZnO nanostructures, theirs structural, morphological, optical, electronic and chemical properties is presented here.

4.3.1.1 Initial oxidation

Similar to the initial oxidation process of Cu thin films (as discussed in Chapter 3), four probe resistivity measurement techniques have also been used to find the minimum required temperature for the initial oxidation of thin Zn films. The details studies of four probe resistivity measurement techniques are already discussed in Chapter 2 (Deposition and Characterization techniques). It can be taken into account that the native oxide formation is very much spontaneous even at room temperature, as soon as the metal film is taken out from the vacuum chamber and exposed to the ambient air. In this study, we find the temperature required to overcome the native oxide barrier for further oxidation of the Zn film. To exclude any artifacts, Zn films are annealed in air as well as helium (*He*) ambient condition and the corresponding surface resistances are compared as a function of annealing temperature. Temperature dependent resistance plot of thin Zn films in air and helium ambient are shown in Figure 4.1. In case of *He* ambient annealing, a linear increase in surface resistance with annealing temperature (*R-T* plot) is clearly observed for temperature up to 140°C which can be attributed to the thermal coefficient of resistivity of Zn. However, for the case of air annealing, a sudden increase in surface resistance is observed above 120°C, which indicates the onset of oxide formation on Zn film surface at this particular temperature. In case of *He* ambient annealing, cooling path (cycle) nicely follows the heating path (linear increases up to 140°C) which further confirms that there are no chemical changes (oxidation) of Zn thin film during *He* ambient annealing process. Hence, we can conclude that the initial oxidation of the Zn film starts at about 120°C. However, this oxidation process is quite slow and mostly affects the top surface layer of the zinc film. Similar type of surface oxidation for copper films have already discussed in earlier chapter and also been reported [31-32].
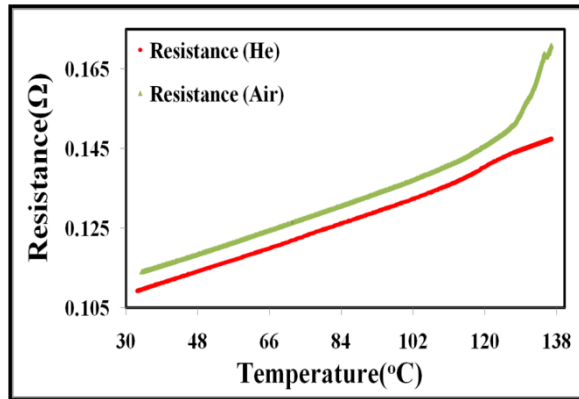
Figure 4.1*: Temperature dependent sheet resistance of Zn thin film during annealing in air and helium (He) ambient.*

4.3.1.2 Temperature dependent oxidation and role of thermodynamics

X-ray diffraction (XRD) studies of thin ZnO films deposited on glass substrate at room temperature are presented in Figure 4.2 to investigate the crystalline quality of the films. As-deposited Zn thin film shows strong diffraction peak (2θ value) centered at $43.45°$, attributed to the (101) reflection plane of hexagonal Zn structure [Figure 4.2 (a,I)]. However, with a little supply of thermal energy a drastic change in XRD pattern is observed, after annealing at 180°C for 4hrs. Two additional diffraction peaks appear at $36.05°$ and $39.8°$, which are originated from (002) and (100) reflection planes, respectively, of hexagonal phase of Zn structure [Figure 4.2 (a,II))]. Surprisingly, no trace of oxide formation is resolved in XRD at this temperature.

Further, increase in oxidation temperature of about 400°C for 4hrs results in ZnO formation with a strong oxide diffraction peaks at 34.33°, which represent the (002) reflection planes of zinc oxide (ZnO) [Figure 4.2(a,III)] [33, 34]. However, the metallic Zn (101) diffraction peak is still visible here. These findings suggest that a significant amount of oxide is only formed after the oxidation temperature is increased to 400°C. Moreover, this oxide layers growth also starts on top of the initial Zn film surface morphology. Further, increase in oxidation temperature up to 500°C for 4hrs results in a very different diffraction patterns with strong and dominating (101) diffraction line of ZnO [Figure 4.2 (b, I)] [33, 34]. In addition, metallic Zn (101) diffraction peak is completely disappeared here, indicating a rapid alteration in initial surface texture of the Zn film. After annealing at around 600°C for 4hrs, (002) plane of ZnO starts to dominate over the (100) and (101) planes of ZnO [Figure 4.2 (b, II)]. This finding can be attributed

126

to another drastic rearrangement of the ZnO film surface textures. In case of oxidation temperature of 650°C for 4hrs, diffraction pattern slightly changes and the ZnO peaks are getting sharpen. A relative decrease in (002) peak intensity is also observed indicating another preferential growth front of ZnO nano-materials [Figure 4.2 (b, III)]. Future, increased in oxidation temperature to 700°C for 4hrs results in a very strong appearance of (101) dffraction line. At the same time (002) peak is almost disappeared suggesting a very different surface texture [Figure 4.2 (b, IV)] [33, 34]. All these XRD results are in good agreement with earlier reported values of ZnO diffraction peak positions [33, 34, 36, JCPDS card No. 79-2205]. These well-defined diffraction peaks are the characteristic of high quality polycrystalline ZnO of hexagonal crystal structure [37]. Improvement in crystalline quality of the ZnO films with increase in oxidation temperature has also been reported by other researchers [38].
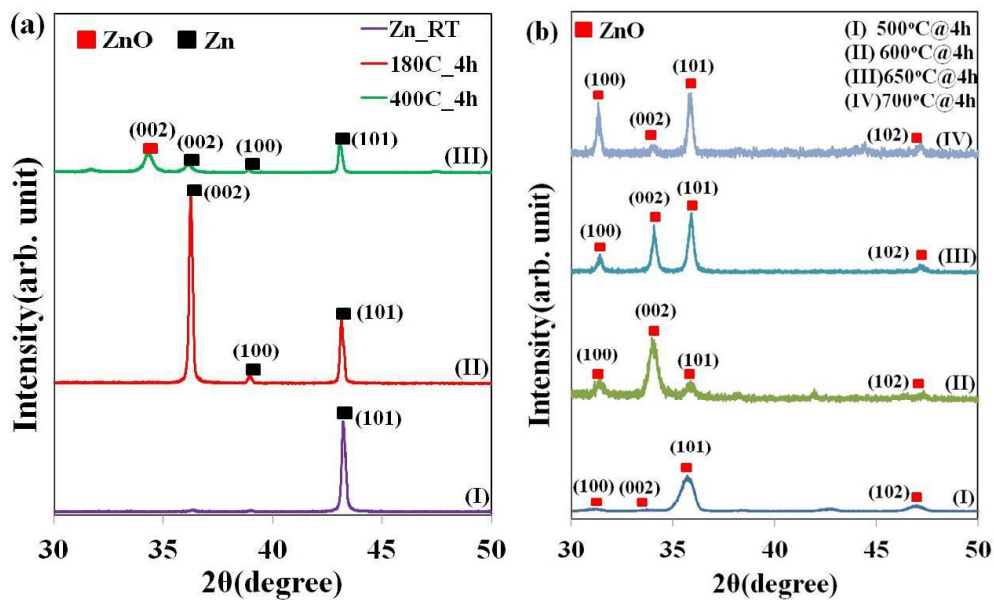

Figure 4.2: *XRD spectra of (a, I) as grown Zn thin films and thermally oxidized at temperatures (II) 180°C, (III) 400°C and (b, I) 500°C, (II) 600°C, (III) 650°C and (IV) 700°C for 4hrs.*

From all these above XRD results it can be concluded that the surface oxidation of Zn film mainly starts above 400°C, while keeping the initial Zn surface morphology unaltered. This can be attributed to a limited thermal diffusion at lower oxidation temperature. With increase in oxidation temperature, thermal energy effectively enhances the surface diffusion process which results in a drastic change in surface

texture of the ZnO film. All these suggested changes in ZnO surface textures are also confirmed with SEM analysisas discussed in following subsection. Therefore, a rapid change in XRD patterns of ZnO films can be correlated to the evolution of a different growth front (surface morphology) of ZnO film. Although the oxidation process of Zn film occurs through the surface diffusion, it is quite obvious that all these changes are very much controlled by the surface thermodynamics as all oxidation steps are sufficiently long up to several hours.

4.3.1.3 Effect of duration and role of diffusion kinetics

The effect of kinetics on the surface oxidation process of thin Zn film is also studied. Similar to copper oxide formation, growth mechanism for ZnO thin films as a function of oxidation time is discussed here using XRD peaks intensity profiles. Starting from the metallic Zn diffraction peaks, stepwise evolution of oxide peaks up to the completion of ZnO phase for different duration (min) of oxidation at 500°C, is shown in Figure 4.3 (I). The XRD patterns of as-deposited Zn thin film appears with strong diffraction peak at 36.28° and 43.45°, representing (002) and (101) reflection planes of Zn, respectively [Figure 4.3 (I,a)]. After 15min of oxidation at 500°C, ZnO phases start to appear at $2\theta = 31.82°$, $34.38°$ and $36.16°$, representing (100), (002) and (101) diffraction planes of ZnO, respectively [Figure 4.3 (I,b)]. Oxide peak correspond to (101) crystal planes of ZnO become relatively stronger after 30min of oxidation. At the same time, diffraction peak corresponds to (101) metallic Zn at $2\theta= 43.45°$ becomes significantly weaker [Figure 4.3 (I, c)]. With duration, oxide phase dominates over the metallic Zn phase and finally completes to the single phase ZnO thin films. After 45min of oxidation XRD peaks related to metallic Zn is completely disappear [Figure 4.3 (I,d)].

For quantitative analysis of the oxide phase formation, Lorentzian profile fit of the Zn (101) and ZnO (101) XRD peaks as a function of oxidation time are displayed in Figure 4.3 (II) and (III). To compare the relative amount of metallic Zn and oxide phase, the intensity (area) ratio of both peaks can be compared. Gradual decrease in Zn (101) peak intensities with gentle increase in ZnO (101) peak intensities is clearly observed as shown in Figure 4.3 (II) and (III), respectively. Assuming a homogeneous layered growth of the oxide phase through the surface diffusion of O_2, a relative depth profile for Zn and ZnO are also estimated as can be seen in Figure 4.4. The relative intensity profile

suggests that the oxide growth is much faster at the initial stage and then slows down with layer thickness and finally terminates. A detailed study of similar kind of work on copper oxide thin films is already described in Chapter 3.
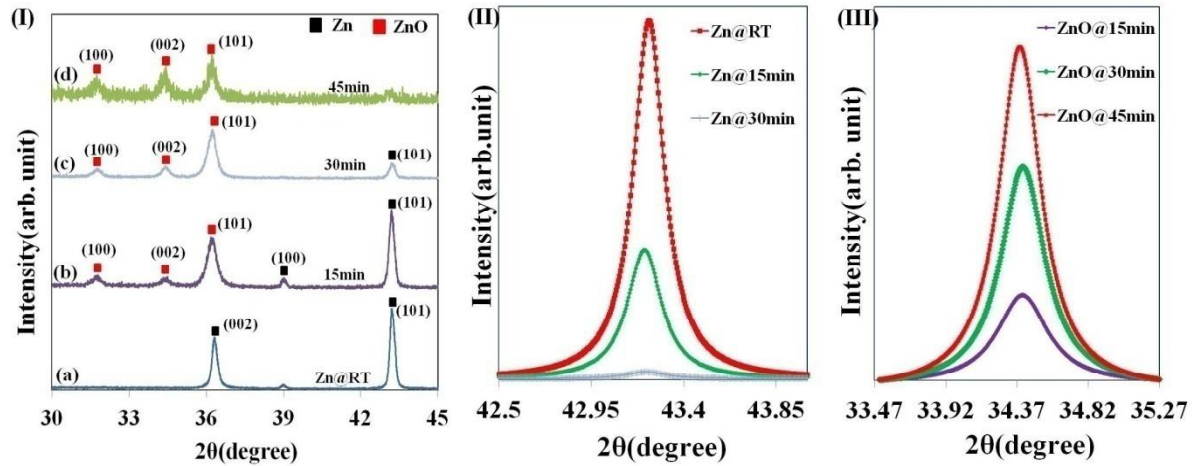

Figure 4.3: (I) XRD spectra of (a) as-deposited Zn thin films and transformation to ZnO phases for durations of (b) 15min, (c) 30min, (d) 45min and Lorentzian fit of XRD spectra (II) Zn (101) and (III) ZnO(101)diffraction peaks as a function of oxidation time during thermal oxidation in air at 500°C temperature.
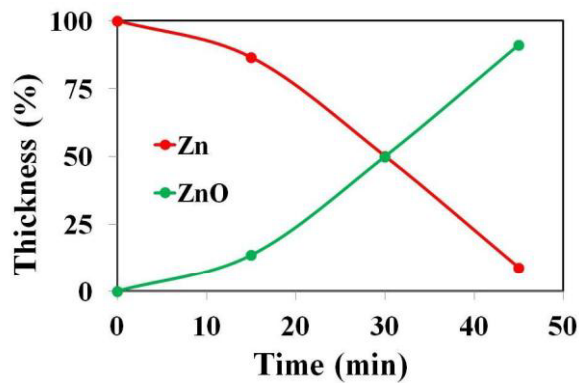

Figure 4.4: Area of Zn (101) and ZnO (101) diffraction lines, along with their oxide growth kinetics.

4.3.2 Characterization of ZnO thin films

Various characterization techniques such as scanning electron microscopy (SEM), transmission electron microscopy (TEM), Raman spectroscopy, X-ray photoelectron spectroscopy (XPS) as well as surface resistivity and Hall measurement have been used

to investigate the surface morphology, crystalline structure, optical, chemical and electronic properties, respectively, of the ZnO thin films.

4.3.2.1 Scanning Electron Microscopy (SEM)

To investigate the surface morphologies of the zinc thin films oxidized at different temperatures (RT–700°C), SEM studies of ZnO surfaces are performed as shown in Figure 4.5. The surface morphology of as-grown thin Zn film shows faceted sidewall morphology of irregular grains [Figure 4.5 (a) & (b)]. Figure 4.5 (c) and (d) represents the SEM image of thin Zn films annealed at 240°C for 4hrs, where 2D vertical growth of nano-wall structures is clearly observed [33,39]. It can be concluded from both SEM and XRD results that (002) plane of metallic Zn is mostly responsible for the vertical growth and nano-wall formation (perpendicular to the substrate surface) is energetically preferable. Figure 4.5 (e) and (f) shows the surface morphology of ZnO film after oxidation at 400°C for 4hrs. Overall surface texture appears quite similar to the nano-well structures observed at 240°C. However, the side wall surfaces of the nano-walls appear significantly rougher after annealing at 400°C. The roughening of the side wall surface might be an indication of oxide phase formation at this temperature, which is complementary with the XRD result [33, 40]. At the same time, overall surface texture follows the initial Zn film morphology due to kinetic limitation of thermal diffusion of oxide species at this temperature. After oxidation at 500°C for 4hrs, a drastic changed is observed on surface morphology of the ZnO thin film. A transition from vertical nano-wall structures to laterally grown nano-sheet surface morphology is clearly observed, which might be thermodynamically more favorable for ZnO films at this temperature [Figure 4.5 (g) & (h)]. This transition process is further continued as lateral growth front dominates over the vertical growth at 600°C [Figure 4.5 (i) & (j)]. Nano-walls are completely deformed and converted into porous nano-sheets at this oxidation temperature [33, 41]. In comparison with earlier XRD results it can be concluded that (002) diffraction peak of ZnO is attributed to the lateral growth of nano-sheet structures. Larger thermal diffusion, facet formation can also play a significant role behind this transion by successfully lowering the overall surface free energy.

130

Morphological evolutions of ZnO films for even higher oxidation temperatures are depicted in Figure 4.6. Further increase in oxidation temperature to $650^{o}C$ appears with another morphological transition of the ZnO films. From a laterally grown homogeneous 2D surface morphology to an asymmetric growth front of 1D nanostructure, leading towards ZnO nano-rods formation is clearly observed [Figure 4.6 (a & b)]. Future increased in oxidation temperature to about $700^{o}C$ for 4hrs accelerates the asymmetric growth of 1D ZnO nano-rods structure at the cost of nano-sheet surface morphology [Figure 4.6 (c & d)] [33, 35]. By the formation of ZnO nano-rods/wires a significant decrease in surface energy can also be expected over the lateral 2D nano-sheets structure [29, 36]. The polar face of ZnO (002) of the nano-sheet has relatively higher surface energy as compared to the non-polar (100) faces. From all XRD and SEM results, it is quite obvious that (002) plane of metallic Zn might be the key element of initial ZnO nano-walls formation and about $500^{o}C$ morphological transition of ZnO films from vertical to lateral growth starts to occur. The homogeneous 2D lateral growth (nano-sheet) can be corellated to the (002) diffraction peak of ZnO whereas assymetric 1D growth (nano-rods) represents the (101) and (100) XRD peaks.

Therefore, both XRD and SEM results are very much complementary with each other for oxidation of Zn films within a temperature range starting from RT to $700^{o}C$ [33]. To exclude any influence of the substrate on ZnO surface morphology, thermal oxidation of thin Zn films deposited on oxidized silicon substrates have also been tested. A very similar kind of ZnO nanostructures morphology is also obtained on silicon substrates, which are depicted in Figure 4.7. As deposited Zn film appears with faceted side wall surface morphology of vertical nanostructures [Figure 4.7 (a)]. Oxidation at $500^{o}C$ results in severe roughening of the sidewall facets leading towards the lateral growth direction [Figure 4.7 (b)]. Oxidation at $600^{o}C$ promotes the 2D lateral growth of ZnO nanostructures.
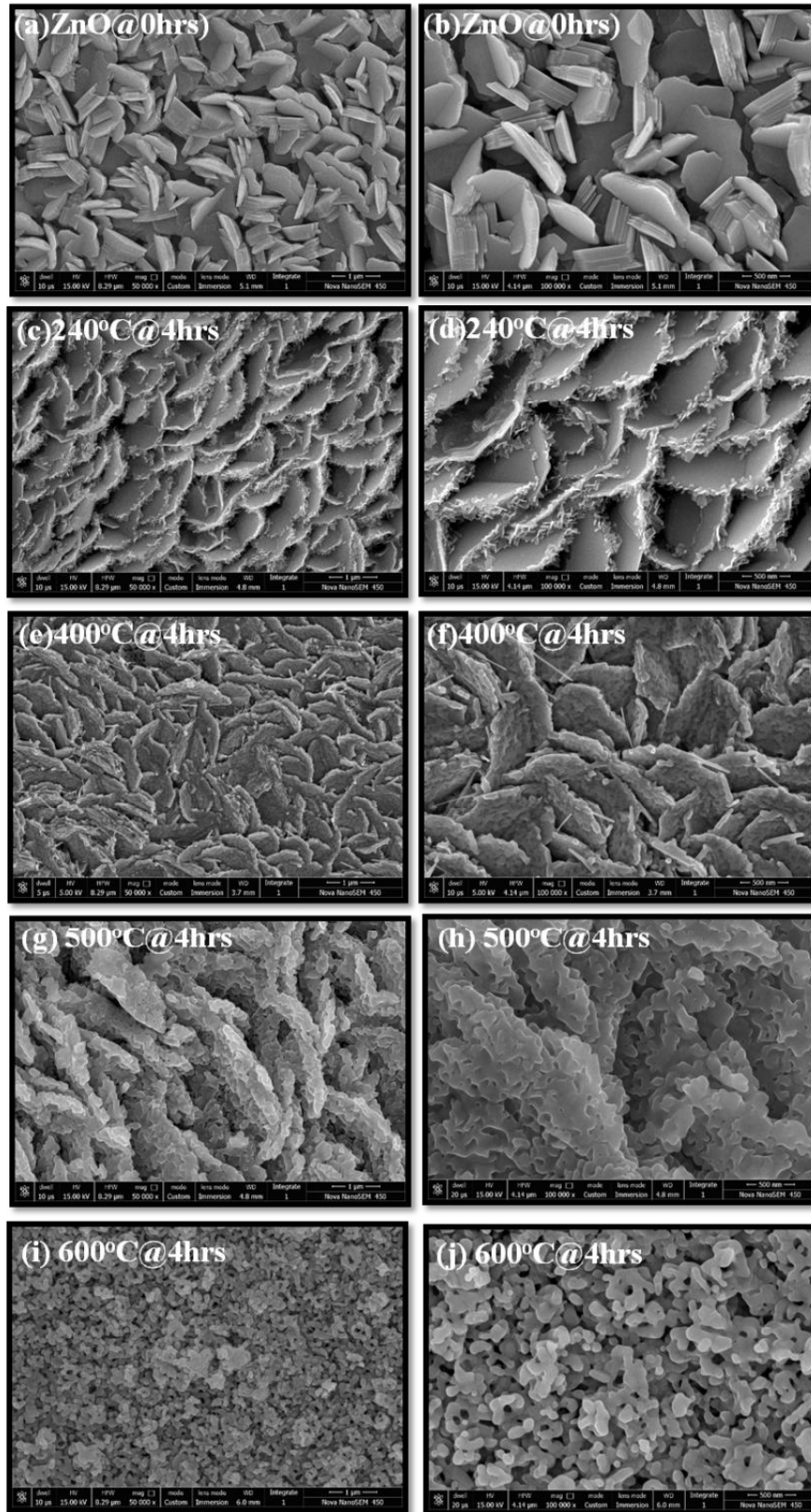
Figure 4.5: *FESEM images of Zn films on glass substrate thermally oxidized at: (a & b) as-grown (c & d) 240ºC, (e & f) 400ºC, (g & h) 500ºC and (i & j) 600ºC for 4hrs. Right column shows a closer view.*
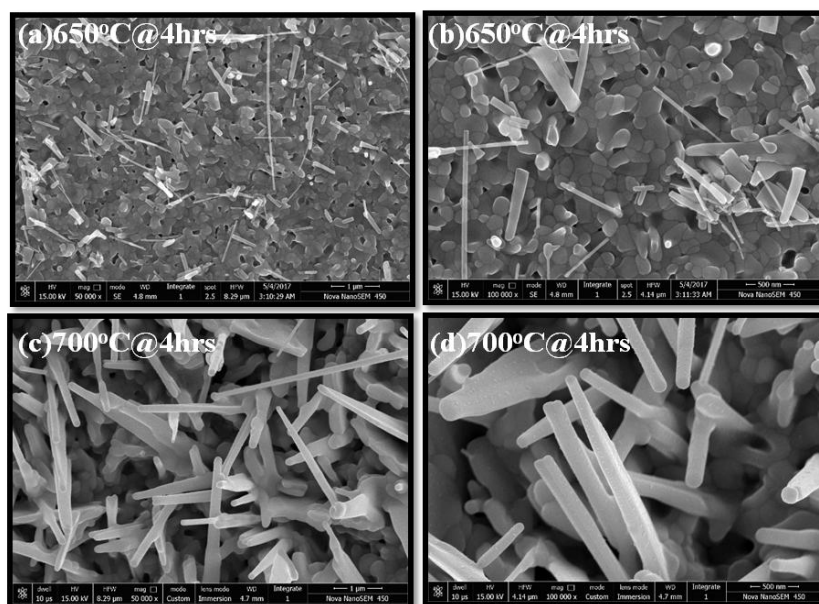
Figure 4.6: *FESEM images of Zn Nano-rods on glass substrate. Oxidation temperature: (a & b) 600°C and (c & d) 700°C. Right column shows a closer view.*

Transition from vertical nano-walls to lateral nano-sheets surface morphology is observed here [Figure 4.7 (c)]. Further increase in oxidation temperature to 650°C initiates another morphological transition, the asymmetric 1D growth and formation of ZnO nano-rods/wires [Figure 4.7 (d)]. The asymmetric transition of 1D nano-rods growth is completed after oxidation of Zn film at 700°C [Figure 4.7 (e)]. By comparing these results with earlier ZnO films grown on glass substrates, it can be concluded that the ZnO surface morphology is very much controlled by the surface kinetics and thermodynamics, whereas the role/influence of the substrate may almost be ignored.
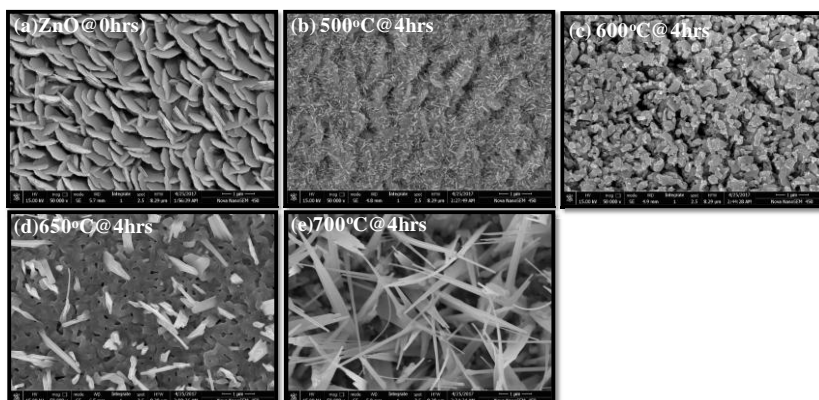

Figure 4.7: *FESEM results of (a) as-grown Zn film and thermally oxidized at (b) 500°C, (c) 600°C, (d) 650°C and (e) 700°C for 4hrs on SiO₂/Si substrate.*

133

A schematic representation of different surface morphology of the Zn thin films, during the thermal oxidation under air ambient is summarized in Figure 4.8. Up to an annealing temperature of 400°C, transformation of metallic Zn to form the nano-wall structure is shown in Figure 4.8(a), where the wall height is increased at the cost of wall thickness. However, above 450°C oxidation process starts and the ZnO exhibits two stages of phase transition: (i) homogeneous 2D lateral growth at 550 and (ii) asymmetric 1D nano-rod growth at 650°C. Detailed understanding of the ZnO nano-rods growth and their morphological changes are discussed in the following TEM section.
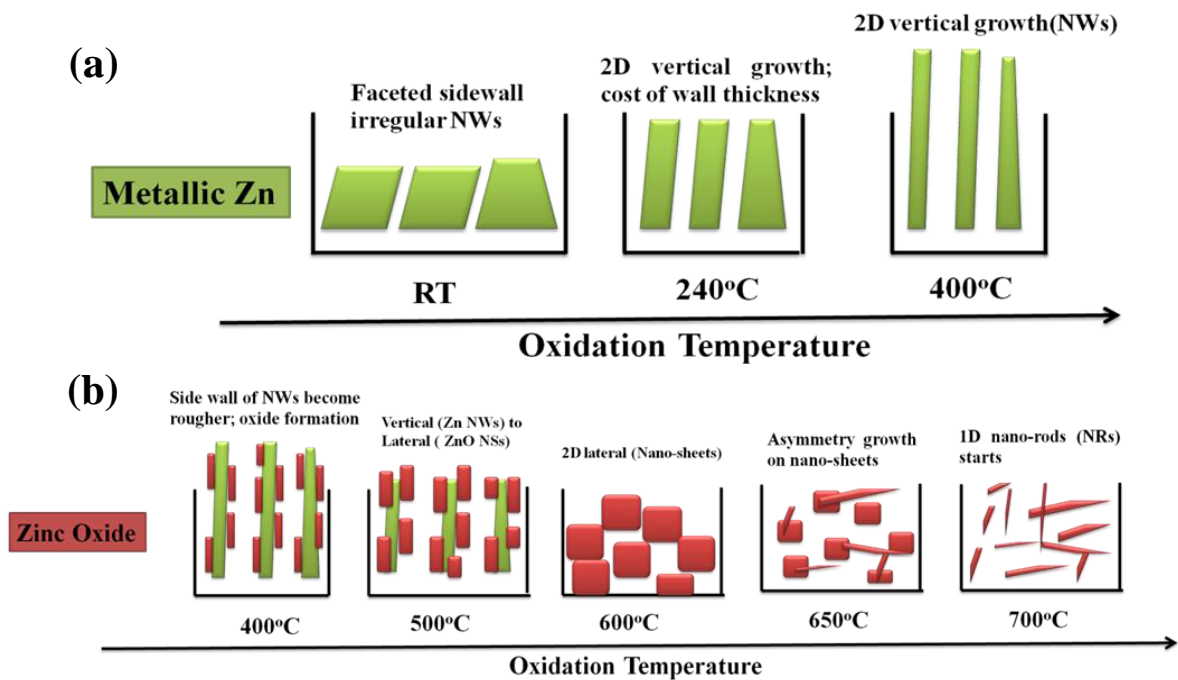

Figure 4.8: A schematic representation of different surface morphologies of (a) the transformation of metallic Zn to ZnO phase and (b) ZnO phases at higher temperatures.

4.3.2.2 Transmission Electron Microscopy (TEM)

For further investigation of the ZnO nano-rods structure, high resolution transmission electron microscopy (TEM) analysis of the ZnO nano-rods film surfaces is also performed. Basically, two different shapes of the nano-rods are found in SEM imaging such as (i) Conical (Pyramidal) and (ii) Cylindrical (Prism). These nano-rods are grown from a 2D Nano-sheet of homogeneous ZnO (002) layer. Growth of ZnO films can be explained in two ways such as isotropic growth with polar (001) facets as well as anisotropic growth with (100) non-polar as well as (101) partially-polar facets. Different crystal planes of typical nano-rods structures are schematically shown in Figure 4.9. In

case of isotropic growth mode, the growth of polar crystal face (001) in the c-axis (fixed crystal orientation) where tetrahedrally coordinated O^{2-} and Zn^{2+} ions, mounted alternatively [42-43]. However, for the anisotropic case, the nucleation can be almost in all direction of ZnO hexagonal plane for both (100) and (101) crystal faces.
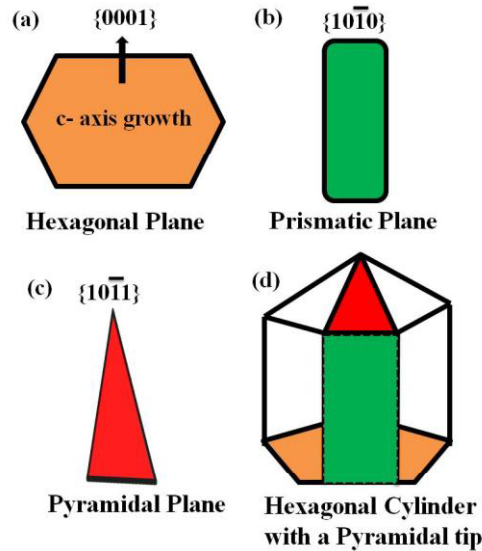

Figure 4.9: *Schematic representation of different crystal planes of a ZnO nano-rod with prismatic and pyramidal facets*

ZnO nano-rods are grown by thermal oxidation of thin Zn films at 700°C for 2 hrs in an air ambient condition. ZnO nano-rods appear with a smooth faceted surface morphology as shown in Figure 4.10. Two different textures, such as (i) Pyramidal nano-rods [Figure 4.10 (a-d)] and (ii) Prismatic nano-rods [Figure 4.10 (e-h)] are generally observed. Typical, SEM images and TEM micrographs of pyramidal and prismatic ZnO nano-rods along with their high resolution TEM images and selective area electron diffraction (SAED) patterns are depicted here. In both cases, the growth direction of the ZnO nano-rods is found to be along the c-axis, i.e., (001) direction which can be derived from the HRTEM images inter plane spacing of Figure 4.10 (c) and (g), respectively. Prismatic ZnO nano-rods exhibits a clear lattice fringes with a lattice spacing of 0.520 nm corresponding to the c-axis spacing of the (0002) atomic planes [Figure 4.10 (g)]. Figure 4.10 (d) and (h) display the SAED patterns for Pyramidal and Prismatic ZnO nano-rods, respectively. Both diffraction patterns are very much complementary with their corresponding pyramidal and prismatic crystal facets formation.
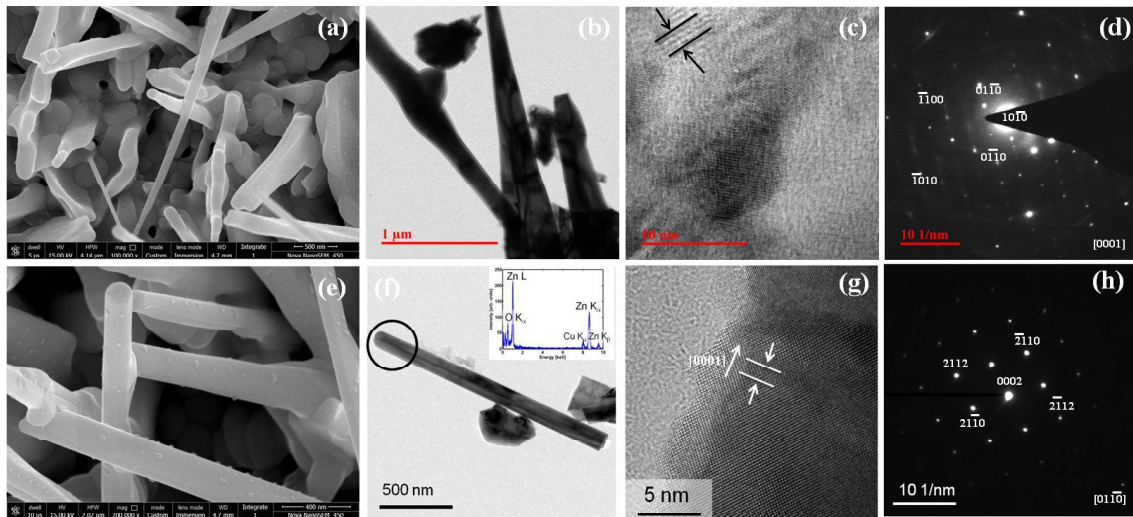
Figure 4.10: *Prismatic ZnO nano-rods: (a) SEM image, (b) TEM micrograph, (c) HRTEM image, (d) SAED pattern, and Pyramidal ZnO nano-rod: (e) SEM image (f) TEM micrograph,(g) HRTEM image (inset shows EDS), (h) SAED pattern.*

This type of characteristic growths is the results of surface energy minimization through different crystal facets formation. The polar faces are having relatively higher surface energy as compared to the non-polar faces [44]. Therefore, wurtzite ZnO nanostructures usually tend to maximize the exposed areas of non-polar facets (lower surface energy) and minimize the exposed areas of c–plane polar facets with high surface energy [43]. Another possible reason which can also influence the growth morphology is the growth rate of any crystal plane. It has been reported that the growth rate of ((001) polar plane is much faster than the non-polar (100) plane [45]. Anisotropic growth of the ZnO crystal along the [001] direction is due to this inherent polar properties of the material. As it a substrate supported growth of ZnO nano-rods and the growth rate of (00-1) plane is much lower as compare to the (001) face, it is assumed that the preferred growth direction is [001] [along [0001] with 4 coordinates system]. The high resolution TEM image and SAED pattern reveal that [001] is the preferred growth direction and the dominating surface area of nano-rods crystal originated from the {100} planes for Prismatic and {101} planes for Pyramidal shapes, respectively [43, 46]. For any pure prismatic nano-rod, the terminating surface is (001), i.e., the c-plane, which has a relatively higher surface energy. At the same time, asymmetric growth with prismatic or pyramidal planes are having a higher surface to volume ratio as compare to (001) plane termination [47]. Therefore, an optimization of the ZnO nano-rod's surface energy can be

achieved by formation of a prism with pyramidal tip as presented in Figure 4.8(d). Therefore, prismatic (cylindrical), pyramidal (conical) and pencil-shaped (combination of both) ZnO nano-rods are expected to grow, perfectly oriented along the c-axis [46].

4.3.2.3 Raman Spectroscopy

To identify the oxide phases of thin zinc films annealed at different oxidation temperatures, Raman spectroscopy has been used as a characterizing tool as shown in Figure 4.11. All Raman spectroscopy measurements are performed within a spectral region of 100-900 cm^{-1}. A strong peak appeared at 563.6 cm^{-1} from the as deposited Zn films is mainly contributed by the metallic phase of Zn which can be explained in the following manner [Figure 4.11 (a)]. The peak at 563.6 cm^{-1} could be the contribution from the E1 (LO) mode of ZnO associated with the oxygen deficiency [48]. Such a strong intensity at 563.6 cm^{-1} indicates that the as-grown Zn film is severely oxygen deficient (*i.e.*, metallic Zn). The intensity of the Raman peak at 563.6 cm^{-1} becomes weaker during increase in oxidation temperatures from 180°C to 400°C [Figure 4.11 (b) – (d)]. In addition, the peak at 563.6 cm^{-1} is also shifted towards a lower value at 554.7 cm^{-1}. Both these findings indicate a reduced oxygen vacancy within the ZnO film by forming the initial oxide layer on top of Zn films, which appeared as a mixed phase of metallic Zn and ZnO [49].
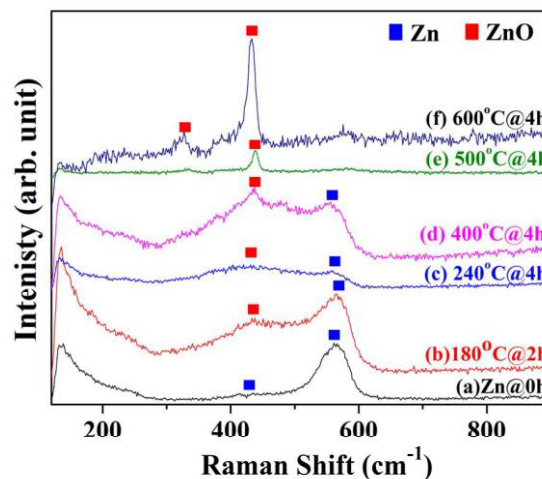

Figure 4.11: *Raman spectra of (a) as grown Zn film and thermal oxidation of Zn films at (b) 180°C, (c) 240°C, (d) 400°C, (e) 500°C, (f) 600°C for 4 hours in air ambient.*

Further annealing at higher temperature (500 - 600°C) shows a single phase of ZnO formation [Figure 4.11 (e & f)]. The broad peaks, associated with the oxygen vacancies of ZnO films are almost disappeared. Moreover, Raman peak at 438.7 cm^{-1} originated from the ZnO E2 mode appears significantly stronger, suggesting a very low oxygen vacancy (pure oxide phase *i.e.*, ZnO). These findings are very much in line with our XRD results. However, XRD could not recognise the oxide formation of the Zn film below 400°C as it not a very surface sensitive technique. Whereas, four probe technique suggests the initial oxidation at about 120°C, which appears in Raman spectra as oxide peak with severe O_2 vacancy.

4.3.2.4 X-ray photoelectron spectrometry (XPS)

In order to analyze the chemical compositions and the defect states of the ZnO thin films, XPS measurements were performed. Typical XPS survey spectrum of ZnO thin film is shown in Figure 4.12 (a). All binding energy positions of the XPS spectra are calibrated using the carbon C1s peak (284.5 eV) as a reference. The survey spectrum of ZnO thin film appears with different binding energy lines of O1s (530.0 eV), Zn 3s (137.8), Zn 3p (86.9), Zn 3d (8.9 eV), Zn $2p_{3/2}$ (1021.7 eV) and Zn $2p_{1/2}$ (1045.2 eV), along with Auger lines of Zn (LMM), Zn (KLL), Zn (LMM_3) [48]. All these binding energy positions are similar to the matrix elements of ZnO wurtzite structure [50]. Figure 4.12 (b) and (c) represent the typical high resolution scans of O1s [Figure 4.12 (b)] and Zn2p [Figure 4.12 (c)] binding energy spectra. High resolution scan of O1s XPS spectrum of the nano-rods ZnO thin films shows a strong asymmetry. The main peak centered towards the lower binding energy (530.9 eV) can be attributed to oxygen atoms within the ZnO lattice whereas weak shoulder at higher energy side can be due to the O-ions, vacancies and contaminants [51]. The binding energy positions of Zn$2p_{3/2}$ and Zn $2p_{1/2}$ appeared at 1021.7 and 1045.2 eV, respectively, which are in agreement with the reported values ZnO [36, 52].

A detailed study of high resolution XPS scans of different ZnO nanstructures is also performed as can be seen in Figure 4.13. The effect of oxidation temperatures as well as the surface texture of different ZnO nanostructures leading to a relatively different stoichiometry are also compared. Both O1s and Zn$2p_{3/2}$ de-convoluted spectra appear

qualitatively similar but there are some significant quantitative differences which are summarize in Table 4.1. Intensity ratio of oxygen species within ZnO crystal (O-crst) to the $Zn2p_{3/2}$ state relatively increases from 0.08 for ZnO film grown at 240°C to 0.13 for 700°C grown films. This is a clear indication of enrichment of oxygen content within the ZnO film grown at higher oxidation temperature. A low *O1s* to *Zn2p₃/₂* peak intensity for 240°C grown films indicates a Zn-rich (metallic) surface whereas a significant increase in the same for ZnO nanostructures grown at 500°C is most likely due to proper oxide formation. However, all Zn_{2p} spectra show a peak intensity ratio of ~2 for triplet (3/2) to singlet (1/2) binding energy states which is nicely matching with the theoretical value. These findings are very much complementary with our electrical characterizations as discussed later and in good agreement with other reported works [36, 53]. For better understanding and clarity, every detail of all of de-convoluted spectra is summarized in Table 4.1.
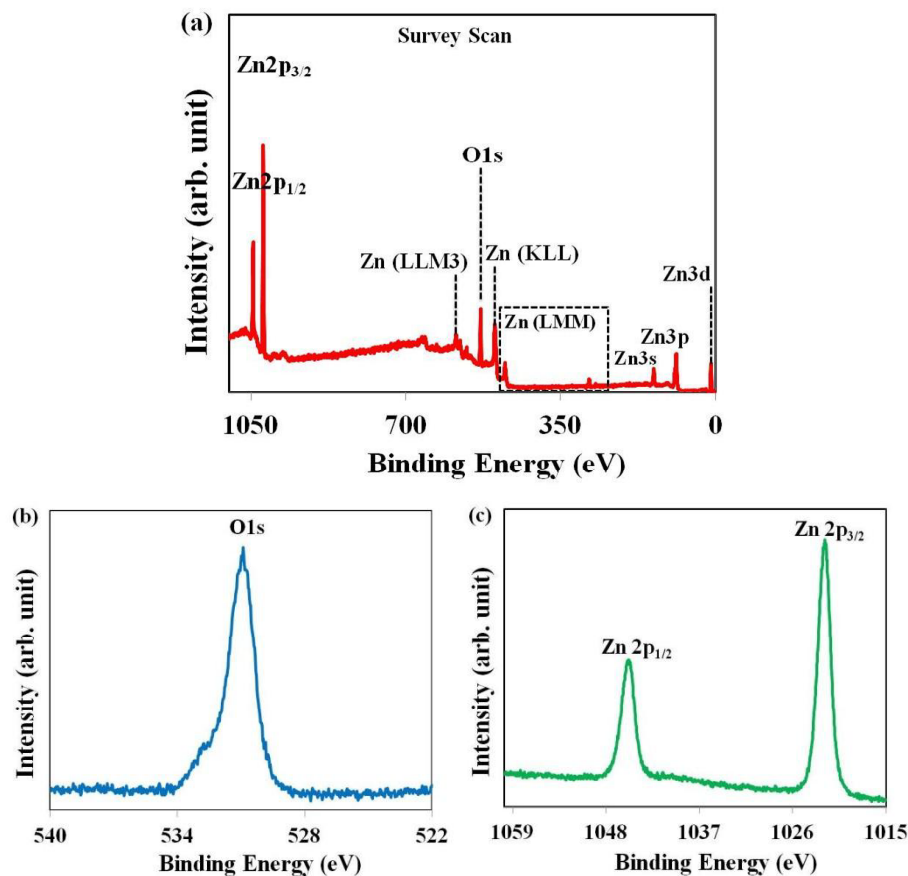

Figure 4.12: *XPS (a) survey scan and high resolution spectra of (b) O1s, (c) Zn2p binding energy peaks of ZnO nano-rods formed after air oxidation of Zn films at 700°C for 4 hours.*
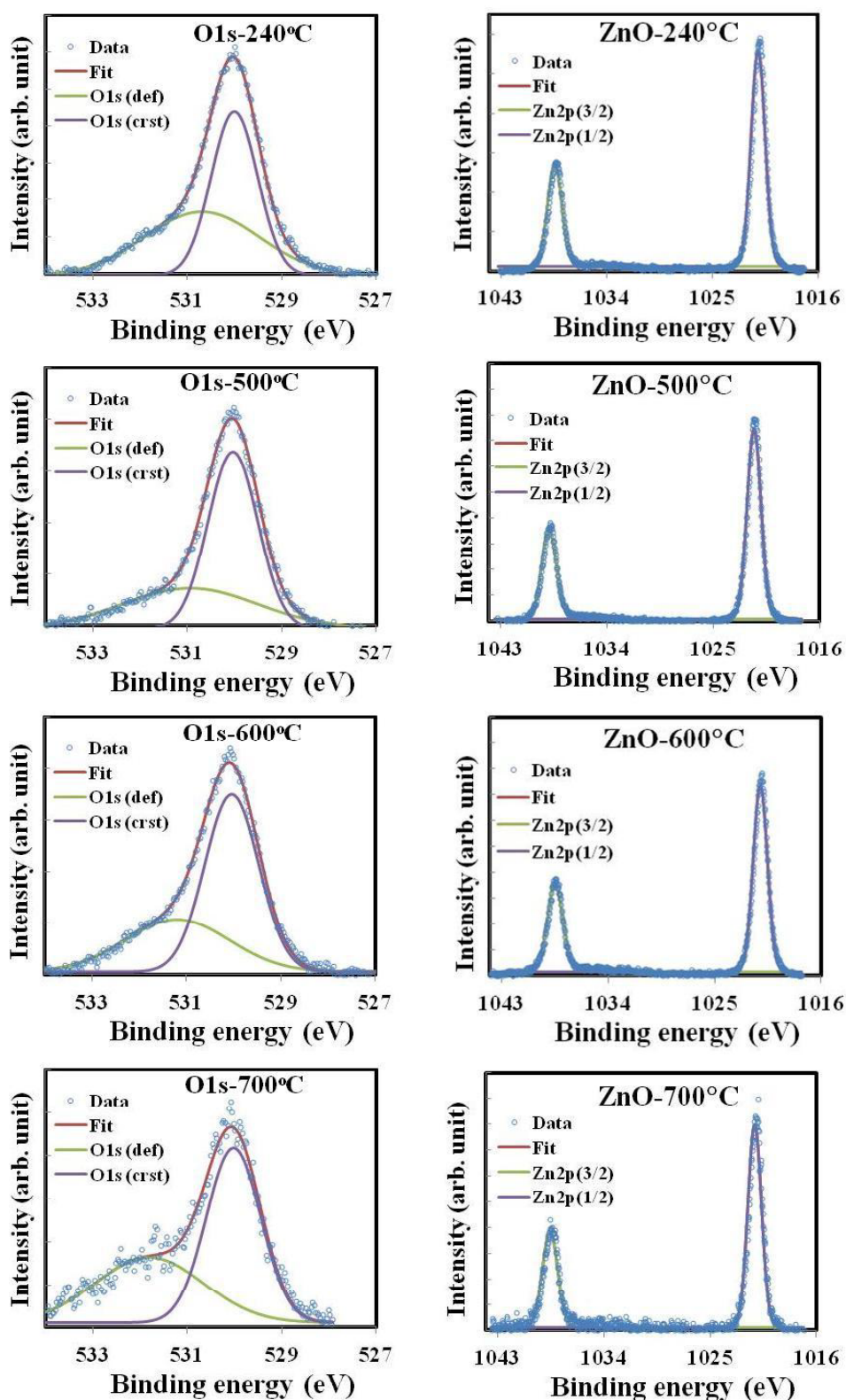
139

Figure 4.13: *High resolution Zn2p and O1s binding energy spectra of ZnO nanostructures grown at different oxidation temperatures.*

Table 4.1: *(a) Binding energy positions and relative peak intensities of deconvoluted O1s and Zn2p spectra of different ZnO thin films. (b) Relative intensity ratio of O-crst vs* $Zn2p_{3/2}$ *and* $Zn2p_{3/2\ to}\ Zn2p_{1/2.}$

Sample name	BE Peak	Sub-peaks	Position	Area
ZnO 240°C	O1s	O-def	530.69	130.9235
		O-crst	529.999	136.4945
	Zn2p	Zn2p1/2	1045.416	793.008
		Zn2p3/2	1021.7	1628.96
ZnO 500°C	O1s	O-def	530.932	68.6275
		O-crst	530.03	113.842
	Zn2p	Zn2p1/2	1045.915	546.571
		Zn2p3/2	1021.574	1094.625
ZnO 600°C	O1s	O-def	531.223	70.5845
		O-crst	530.07	123.3075
	Zn2p	Zn2p1/2	1045.531	556.448
		Zn2p3/2	1021.176	1080.132
ZnO 700°C	O1s	O-def	531.813	22.171
		O-crst	530.025	29.577
	Zn2p	Zn2p1/2	1045.55	122.598
		Zn2p3/2	1021.204	228.913

Ratio 1	ZnO 240°C	O-crst	Zn2p 3/2	0.08379242
	ZnO 500°C	O-crst	Zn2p 3/2	0.10400091
	ZnO 600°C	O-crst	Zn2p 3/2	0.11415966
	ZnO 700°C	O-crst	Zn2p 3/2	0.12920629
Ratio 2	ZnO 240°C	Zn2p 3/2	Zn2p 1/2	2.053
	ZnO 500°C	Zn2p 3/2	Zn2p 1/2	2.003
	ZnO 600°C	Zn2p 3/2	Zn2p 1/2	1.941
	ZnO 700°C	Zn2p 3/2	Zn2p 1/2	2.044

From all XPS observations it is quite obvious that increase in oxidation temperature results in an enhanced O_2 species within the ZnO film. It is by nature an n-type semiconductor which can be explained in terms of O_2 vacancy model. A relative

increase in O_2 species within ZnO will resultantly reduce the O_2 vacancy formation. Therefore, a diminished carrier (electron) concentration for ZnO is expected for higher oxidation temperature. Therefore, an increase in surface resistivity for ZnO film grown at higher oxidation temperature is also predicted which is very much complementary with our electronic properties characterization results [54]. Finally, it can be concluded that the nano-rods are made of pure ZnO with only a few oxygen vacancies.

4.3.2.5 Four probe measurements

Four probe characterizations techniques are used to investigating the various electrical properties of metal oxide thin films such as resistivity (ρ), carrier mobility, carrier concentration, hall coefficients etc.

Four probe resistivity measurement

The surface electrical resistivity of nano-structured ZnO thin films is characterized using four probe resistivity measurement techniques. Figure 4.14 shows the I-V measurement of nano-structured ZnO thin films, prepared at different oxidation temperatures under air ambient annealing. The current (I) − voltage (V) measurements taken in the configuration are already described in the chapter 2. In general, Zn films oxidized at 400°C for couple of hours show very high conductivity and almost behave like a metal (not shown within figure). Zn thin films oxidized at 500 °C shows the highest slope, indicating the lowest surface resistance. However, the slopes dramatically decrease with increase in oxidation temperature suggesting higher surface resistances of ZnO thin films grown at 700°C. Hence, we can conclude that the resistivity of the ZnO films obtained by I–V characterization shows a trend to decrease with the annealing/oxidation temperature increases from 500°C to 700°C [55-56].
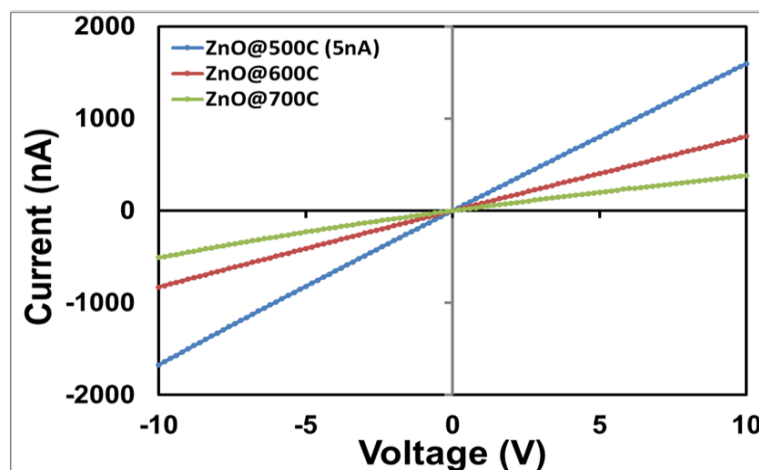
Figure 4.14: *Current – voltage plot of ZnO thin films, prepared at different temperatures during the air annealing.*

Hall Effect

In addition to electrical resistivity measurement, Hall measurements of ZnO films using Van der Pauw method are also performed to get the informations about surface and bulk resistivity, carrier concentration and their mobility, as summarized in Table 4.2. Similar to I-V measurements, resistivity of ZnO films increased with oxidation temperatures. A sudden jump in surface resistivity of nano-structured ZnO thin films from 1.43×10^{-5} Ω-cm at 400°C to 2.6×10^{-2} Ω-cm at 500°C can clearly be observed from Table 4.2. Surprisingly low resistivity and extremely high carrier concentration for 400°C samples indicates that the film is highly metallic (Zn) in nature whereas a drastic jumps/drops for the same at 500°C suggests the oxide (ZnO) formation. These findings are very much complementary with our XRD and SEM analysis. An increase in surface resistivity and Hall mobility, and decrease in carrier (electron) concentrations are also observed with increase in oxidation temperature to 700°C [57]. Decrease in electron concentration with oxidation temperature can be correlated to the O_2 vacancy model described by *Kroger–Vink* (KV) notation, as discussed in the following. However, the rise in carrier mobility may be attributed to the reduction in carrier scattering due to their less numbers. All these findings finally result in an increase in surface resistance for ZnO films, oxidized at higher temperature. It is to be considered that further increase in oxidation temperature beyond 1100°C may cause an outer diffusion of O_2 atoms from the oxide species which may result in thermal decomposition [58].

Table 4.2: *Hall data of ZnO thin films grown at different oxidation temperatures for 4hrs*

Sample Name (growth temp)	Carrier type	Resistivity (Ω-cm)	Hall Mobility (cm^2/V-s)	Carrier (electron) concentration (cm^{-3})
(I) 400°C	n	1.43×10^{-5}	1.745	2.51×10^{24}
(II) 500°C	n	2.6×10^{-2}	3.82	63.91×10^{19}
(III) 600°C	n	4.1×10^{-2}	22.77	6.67×10^{19}

The conductivity of pure ZnO thin films is usually ascribed both to oxygen vacancies [59] or zinc interstitials defects [60], which can be explained in terms of KV notation. This notation is useful for describing various defects structures and may significantly alter on grain size. Following notations are usually used for different atoms or defects such as *i* for interstitial site, *Zn* for zinc, *O* for oxygen and *V* for the vacancy. These terms indicate the atomic sites, and a dot (.) indicates a positive charge whereas a prime (') indicates a negative charge and cross (×) indicates a zero/null charge for ZnO nano-structures. Surface defects and textures (higher surface-to-volume ratio) in ZnO nano-structures play an important role in controlling the properties. There are a number of intrinsic defects in ZnO nano-structures with different ionization energies. Because of their different ionization energies, the relative concentrations of the various defects strongly depend on the temperature. However, the partial pressure of oxygen and zinc (notified as pO_2 and pZn respectively) may also play a significant role on defects formation. *Zn* interstitials and O_2 vacancies are the predominant ionic defect in ZnO nanostructures. At high oxidation temperatures, oxygen vacancies may predominate, which is basically depending on the relative ratio of pO_2 and pZn. Zn may also evaporate during annealing in a Zn-poor environment (air ambient), even at a temperatures as low as 500°C for only a matter of few hours. Hence, ZnO nanostructures grown using air ambient annealing are expected to be mostly with O_2 vacancies. However, Zn interstitial defects are predominant under Zn vapor rich environments. In order to maintain Zn interstitial defects, annealing is required in presence of Zn vapor. Even for similar concentrations, the ionization energy of oxygen (doubly charged) vacancy is lower than that of Zn interstitial. It is also very important to note that the kinetics of oxidation or de-oxidation are relatively slow and at very reducing conditions oxygen vacancy concentration is not easily changed at <1000°C [58]. In addition to defect mechanisms, the electrical properties of polycrystalline films may also be defined by the magnitude of inter-grain back-to-back Schottky barriers [61]. Therefore, a decrease of electron

concentration by itself can be related to the increase of the potential barrier magnitude. However, the decrease in electron concentration with increase of the potential barriers is also accompanied by the dramatic decrease of the mobility. Similar type of study on thin ZnO films is also observed in Ref. [57].
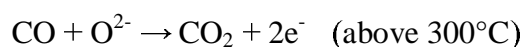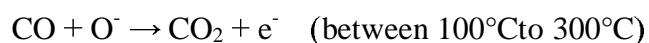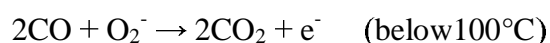
4.4   Gas sensing of nano-structured ZnO thin films

ZnO is a versatile material for various useful applications in different aspects of devices. In addition, ZnO is also a potential candidate for various gas/vapour sensor applications. Within this present work, variety of ZnO nanostructures are grown using thermal oxidation of Zn thin films at air ambient. XRD, Raman spectroscopy and XPS give the confirmation of single phase of ZnO and SEM study revealed that these ZnO thin films are having various type of nano-structured (nano-walls, nano-porous and nano-rods) with a high surface to volume ratio. Especially for the gas sensors applications, various nano-structured ZnO thin films as nano-rods and nano-porous structure is preferred due to their high surface to volume ration. It is also known that the sensitivity and response time of any MO (ZnO thin films) based sensors may strongly be affected by its nano-structures.

Gas sensing mechanism of ZnO nano-structures usually belongs to the surface-controlled reaction (surface - volume ratios) in which the adsorption of oxygen plays an important role. Within this work, two different ZnO surface morphologies such as laterally grown 2D ZnO nano-porous surface and asymmetrically grown 1D nano-rods are preferred for the creation of high efficiency gas sensors. Both films appear with significanlty high surface resistivity and show a high surface to volume ratio. CO gas sensing experiments (resistive) of ZnO nanostructures were performed in a dynamic gas flow mode for different temperatures (150°C-280°C) and CO gas concentrations (50 ppm to 320 ppm). However, for ethanol vapor, static mode of resistive sensing was used at room temperatures. For gas/vapour sensing measurements, thin layer of gold (~100 nm) was deposited on ZnO nanostructures as top electrodes, using vacuum assisted thermal evaporation through a figure mask. Gas sensor setups with appropriate details are already depicted in Chapter 2.

4.3.1 CO gas sensing

The common sensing mechanism of n-type semiconductor (ZnO) involves in formation of a charge depletion layer on the oxide film surface due to the electron trapping by adsorbed oxygen species [62-63]. ZnO is an intrinsic n-type semiconductor due to the oxygen vacancies and interstitial zinc defects. In presence of dry air flow oxygen molecules are generally chemisorbed onto the ZnO surface in the forms of different oxygen ions such as O^{-2}, O^- and O_2^-. However, reducing gas (CO) exposure results in adsorption/desorption reactions lead to the release of the trapped carriers (electrons for n-type) and thus results in a decrease in surface resistivity.Therefore, when the reducing gases (CO) are injected into the chamber, CO gas reacts with the adsorbed oxygen ions and release electrons to the conduction band. As a result, decreases the resistance is observed for nano-structured ZnO thin films. However, the appropriate reaction mechanisms on ZnO surface for different temperature regimes have been reported by *Takata et al.* [64] is given below.

$$2CO + O_2^- \rightarrow 2CO_2 + e^- \quad (\text{below}100°C)$$
$$CO + O^- \rightarrow CO_2 + e^- \quad (\text{between } 100°C \text{ to } 300°C)$$
$$CO + O^{2-} \rightarrow CO_2 + 2e^- \quad (\text{above } 300°C)$$

At lower temperature CO molecules do not have enough thermal energy to react with the surface adsorbed oxygen species. As a result, a significantly high resistance has been observed below 100°C [64].

When an n-type semiconducting (ZnO) surface with electrons as majority carrier is exposed to dry air, oxygen molecules are adsorbed on its surface to produce oxygen ions (O^{2-}, O^-, or O_{2-}) by capturing these electrons from the surface. This capture resultantly leads to the formation of a depletion layer (a decrease in carrier concentration) on the ZnO surface, which further leads to increase in surface resistivity. Now, further exposure to any reducing gas/vapour (CO, ethanol), the pre-absorbed ionized oxygen species on film surface react with the target gas molecules and release back the absorbed electrons. As a result, surface carrier (electron) concentration of ZnO increases and therefore the resistance of the semiconducting surface (ZnO-based sensor) decreases upon exposure with CO gas [65]. However, a completely reverse scenario is expected for an oxidizing gas/vapour [Figure 4.15].
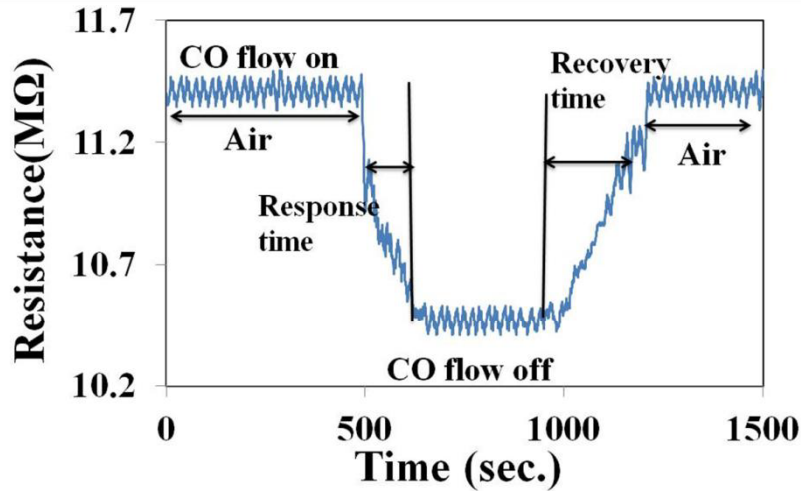
Figure 4.15: *Schematic of response and recovery times of a ZnO thin film based sensor in the exposure of CO gas.*

The sensitivity 'S' of any sensor is generally defined in the form of $S = \Delta R/R_a$, where, $\Delta R = |R_a - R_g|$, R_a and R_g are the sensor resistances in air ambient and in target gas (CO) ambient, respectively [66]. The sensitivity of ZnO thin film sensor strongly depends on the operating temperature and the concentration of the CO gas. Two significantly different morphologies of ZnO nanostructures such as (i) **nano-rods (Sample I)** and (ii) **nano-porous (Sample II)** surfaces are used for the CO sensing studies here. Time dependent surface resistance of ZnO nano-structured thin films based CO sensors for various CO concentrations (50 ppm to 320 ppm) are shown in Figure 4.16 (a-c) (Sample I) and Figure 4.17 (a-c) (Sample II). Three different operating temperatures are compared for both ZnO based CO sensors. A gradual increase in sensing response up to a certain value of the CO concentration is observed for all samples where the response reaches the maxima. For a further increase in CO concentration CO response starts to decrease. Figure 4.16 (a-c) depicts the dynamic responses curve of Sample I at operating temperatures of 200°C, 250°C and 280°C, for different CO concentrations (50-320 ppm). Sample I based sensor shows a gradual increase in CO sensitivity from up to 220 ppm, afterwards a decrease in CO sensitivity for further CO concentration is clearly observed. All responses show a maxima at a CO concentration of 220 ppm for all operating temperatures. Maximum responses of 19.00%, 20.25 % and 5.22% are observed for Sample I based CO sensor operating at temperatures of 200°C, and 280°C, respectively [Figure 4.16 (d-f)]. Therefore, it can be

concluded for Sample I (ZnO nano-rods based CO sensor) that a maximum response of 20.25% can be achieved for a CO concentration of 220 ppm and operating temperature of 250^oC.
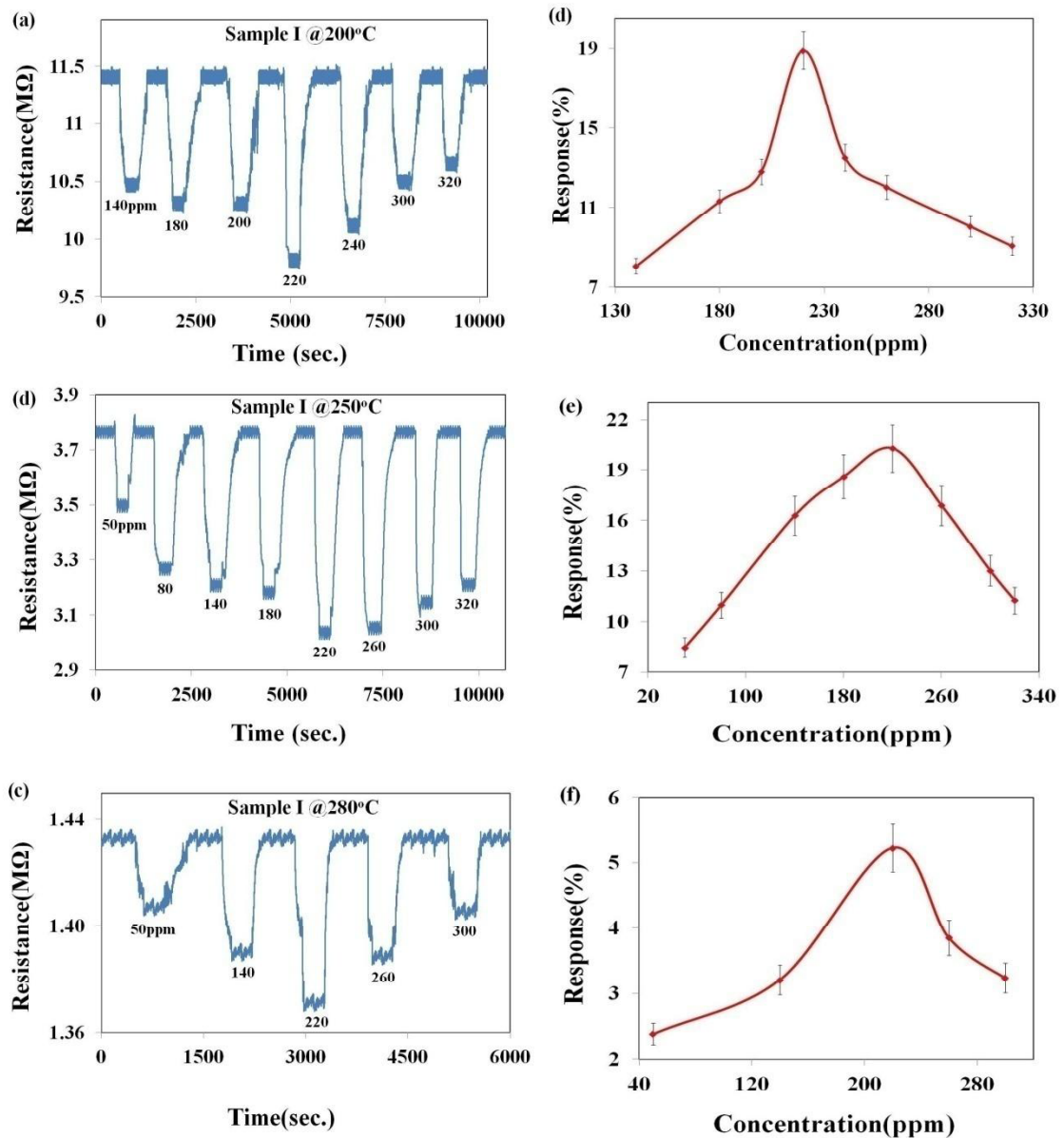

Figure 4.16: Responses curve of Sample I at different operating temperature (a & d) 200^oC, (b & e) 250^oC and (c & f) 280^oC for various concentrations of CO gas.

To compare the sensing performance of various nano-structured ZnO thin films, Sample II has also been tested for CO sensing. Figure 4.17 (a-c) shows the CO responses of the ZnO nano-porous film at three different operating temperatures of 150^oC, 200^oC and 250^oC, respectively. CO gas concentrations are also varied within a range staring

from 100 ppm to 320 ppm. Similar to Sample I, all responses show maxima but with a slightly higher CO concentration of 250 ppm. In addition, a gradual increase in maximum CO response is also observed with the increase in operating temperatures, up to 250°C. Figure 4.17 (d) shows the response of Sample II at 150°C operating temperature where a maximum response of 4.04% is observed. Maximum CO response increases to 6.5% [Figure 4.17(e)] and 7.5% [Figure 4.17 (f)] for operating temperatures of 200°C and 250°C, respectively. However, further increase in operating temperature starts to reduce the maximum response value. Hence, Sample II (ZnO nano-porous film based CO sensor) shows the highest response of 7.5% at 250°C operating temperature for a CO concentration of 230 ppm.

Highest sensing response of ZnO nano-structures based CO gas sensor is observed at an operating temperature of 250°C which can be explained in the following manner. In general, the overall resistive response magnitude (RRM) of metal oxide sensors is considered to depend upon multiple parameters such as operating temperature (T), concentration of target gas molecules (N_g), free charge carriers upon exposure to the target gas (N_e), number of oxygen ions per unit area (N_O), reaction rate constant (*K*) and effective surface area of the oxide nano-structure (Ø) as given by

$$RRM = f\left(\frac{K\emptyset N_O N_g}{N_e}\right) \text{ , where } K = A exp\left(-\frac{E_a}{k_B T}\right)$$

Here, *A* is a time constant and E_a denotes the activation energy. Usually, both reaction rate constant and concentration of free charge carriers get increased with temperature. Hence, the sensitivity of ZnO based CO sensor can highly be influenced by the operating temperature mainly due to two mechanisms: (a) surface adsorption and desorption process and (b) surface chemical reaction. Surface adsorption-desorption mechanism of CO molecule itself is a temperature sensitive process. In addition, depending on the operating temperature initial ZnO surface can offer three different types of surface interaction sites for CO molecules such as O_2^- , O^- , or O^{-2}, adsorbed on ZnO surface. Therefore, CO adsorption process is initially increased with the operating temperature and reaches a maximum. At the same time, CO induced surface chemical reaction (i.e.,$CO + O^- = CO_2 + e$) is also sensitive to the operating temperature as it is found to be an endothermic process for the initial stage. Therefore, the CO adsorption-desorption process and the surface chemical reaction towards CO_2 formation are very much coupled

and are finally optimized to an operating temperature of 250°C for ZnO based sensor. Similar type of explanation is also applicable for the CuO based sesors for CO sensing.
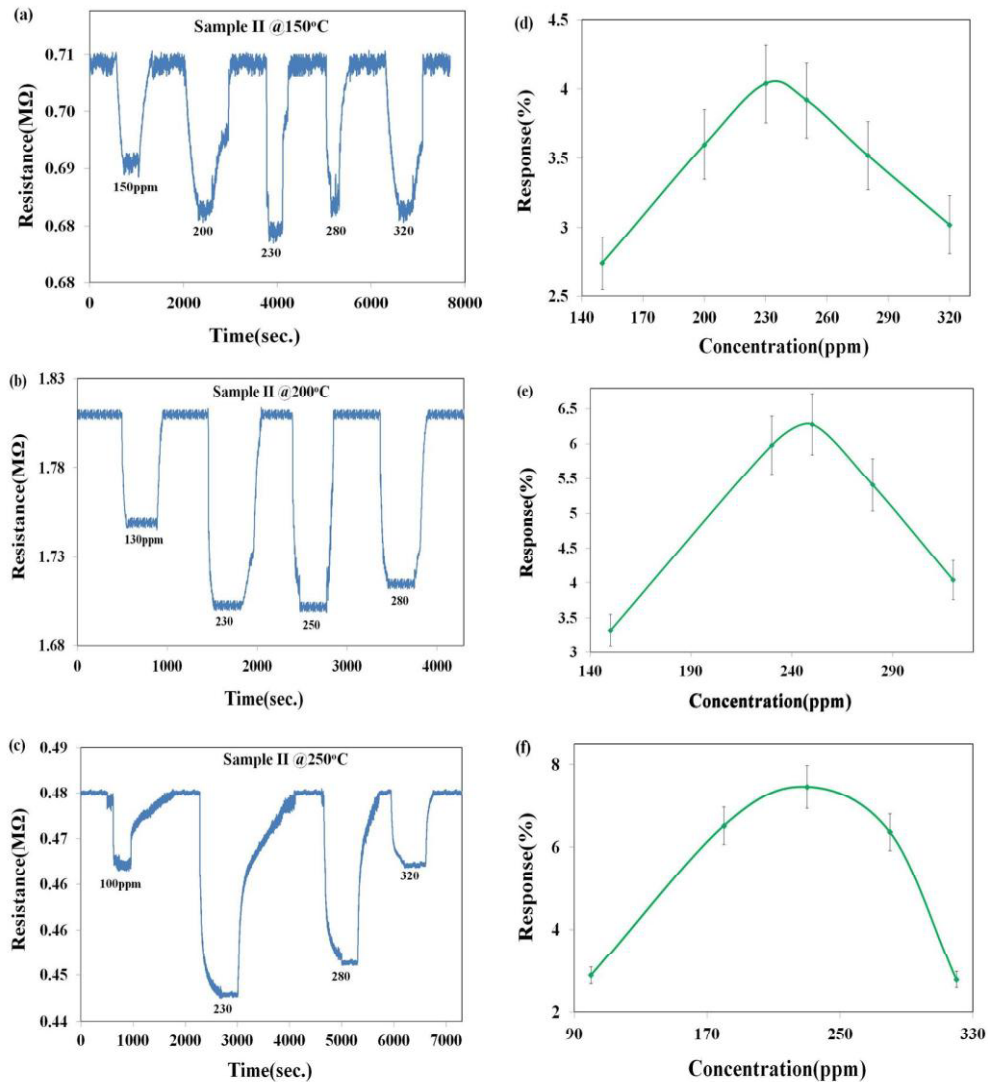

Figure 4.17: *Response curves of Sample II at different operating temperature (a & d) 150°C, (b & e) 200°C and (c & f) 250°C for various CO concentrations.*

A relative comparison of CO sensitivity for both sensors is depicted in Figure 4.18. By comparing both sensing results it is quite clear that the nano-rods (Sample I) based CO sensor appears to be superior as compared to the nano-porous (Sample II) based sensor. ZnO nano-rods based sensor shows maximum CO sensitivity of 20.25 % at 220 ppm, whereas nano-porous ZnO film shows a maximum response of 7.50% at 230 ppm of CO concentration. Surprisingly, the optimum operating temperature for both sensors is found to be 250°C. The highest sensitivity of the ZnO nano-rods sensor may be attributed to its larger surface to volume ratio, which is complimentary with the SEM and XRD results

150

and the presence of less number of surface states or trap centers on ZnO film surface. In addition, point defect in ZnO may also affect the gas sensing measurements, which are already explained from I-V measurement [Figure 4.14]. Finally, the reduction in sensitivity at higher CO gas concentration (above 220 ppm for Sample I and 230 ppm for Sample II) might be attributed to the difficulties in exothermic CO gas adsorption process [67].
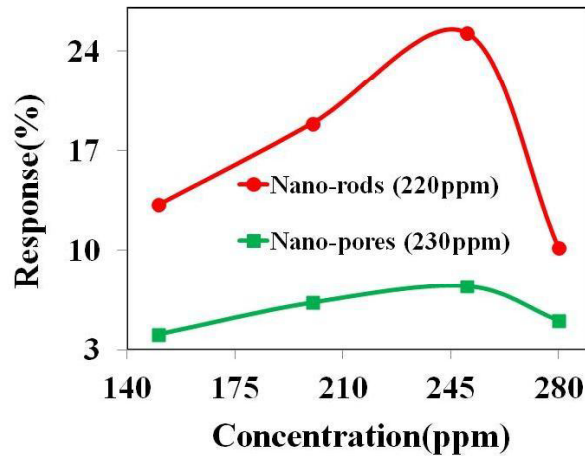

Figure 4.18: *Response curves of nano- structured ZnO thin films based sensors at operating temperature 250°C for maximum concentrations of CO gas.*

4.4.2 Ethanol vapors sensing

ZnO nano-rods based sensor has also been tested in static mode using volatile organic vapor (VOC) such as ethanol. Effect of ethanol vapour on ZnO nano-rods is performed using resistive mode analysis. Most excitingly, all these sensing experiments are conducted at room temperature, without supplying any external heating component. Figure 4.19 shows the ethanol sensing response of ZnO nano-rods surface at room temperature. Two different ethanol vapor concentrations of 2000 and 5000 ppm are used here. The effective surface resistance of ZnO nano-rods significantly reduces in presence of ethanol vapour. In addition, 5000 ppm shows a larger response as compared to 2000 ppm, indicating an enhancement in sensing response with increase of the ethanol concentration.

A similar kind of sensing mechanism can be used to explain the ethanol vapour sensing of the ZnO nano-rods at room temperature, as explained here [68-69]. Resistive response of ZnO nano-rods sensor principally depends on the depletion layer width on

nano-rods surface. It is a function of surface carrier concentration at different ambient like in air and in ethanol vapor.
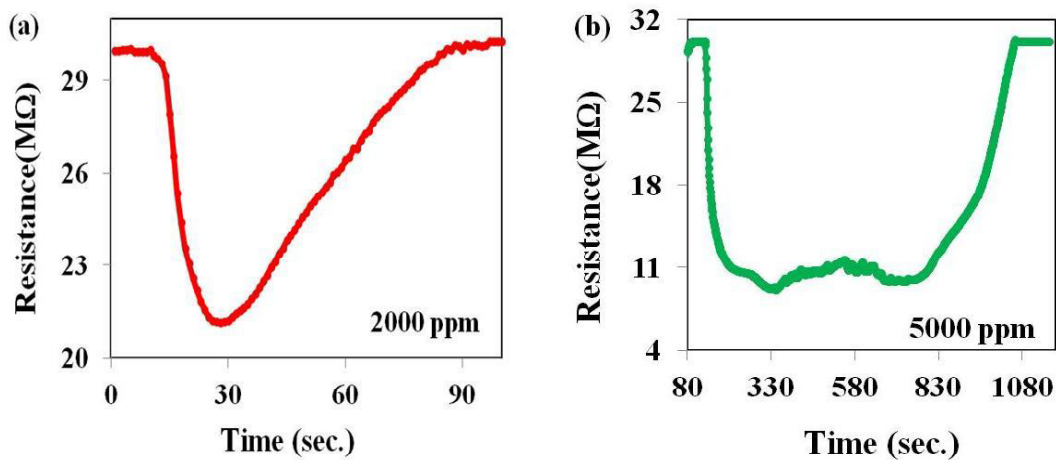

Figure 4.19: *Ethanol vapour sensing at the concentration of (a) 2000ppm and (b) 5000ppm of ZnO nano-rods sensor at room temperature.*

In air ambient, surface free electrons of ZnO nano-rods are trapped by the oxygen species present in air. Surface reaction of ethanol vapor successfully releases the free electrons to the ZnO nano-rods surface, as can be seen in equation:

$$C_2H_5OH + 6O^- \rightarrow 2\ CO_2 + 3\ H_2O + 6\ e^-$$
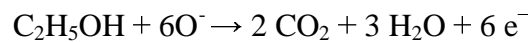
As a result, the thickness of the surface depletion layer reduces and hence the surface resistance). Where, the resistance of ZnO nano-rods deceases with the concentration of ethanol vapour due of the adsorbed oxygen ions on the surface. Finally, ethanol sensing at room temperature can drastically reduce the power consumption of the sensor device, which would be of great technical importance.

4.5 SUMMARY

Controlled formation of different ZnO based nano-structures, their analytical characterizations and finally successful implementation towards the gas sensor fabrication for CO and ethanol vapour have systematically been studied. Both XRD and SEM analysis suggest high quality, crystalline ZnO films can be formed even on glass substrate. Oxidation temperature of the Zn film is found to be very much sensitive towards the formation of ordered nanostructures of ZnO. By systematically controlling the surface

kinetics and diffusion thermodynamics, different ZnO nanostructure growth morphology can be achieved. Vertical growth morphology of ZnO nano-wall/ sheet structures is usually formed at relatively lower oxidation temperature, below 450°C. This vertical is mostly controlled by the kinetics and initial metal Zn film morphology. With increase in oxidation temperature, a transition from vertical to lateral growth morphology of 2D layered structure is observed at around 500°C which is mostly dominated by the thermodynamics. Finally asymmetric growth of 1D ZnO nano-rods/ wires growth at 700°C have been observed which is controlled by the surface free energy of crystal facets/planes. TEM results revealed that ZnO nano-rods are basically of pyramid and prism types with growth direction along the (001) lattice planes. I-V results and Hall measurements have confirmed a significant increase in surface resistivity of ZnO films oxidized at higher temperature. XPS results show a relative enhancement of O$_2$ composition within the ZnO layer for higher oxidation temperature which can successfully explain the electrical properties of reduced carrier concentration and higher sheet resistance. Overall, a nice correlation between structure, morphology and chemistry of different ZnO nanostructures are also discussed.

Afterwards, ZnO thin film based CO gas and ethanol vapour sensors are successfully fabricated by vacuum deposited Au contact electrodes formation on top of the oxide surface. CO sensing result is found to be very much promising for ZnO nano-rods films grown at relatively higher oxidation temperature (700°C). Sensing properties of the ZnO nanostructures are explained in terms of surface adsorption (morphology) as well as its electrical transport properties (resistivity, carrier concentration etc). A significantly enhanced CO gas sensitivity (19%) was obtained at a relatively lower temperature of 200°C for 220ppm of CO concentration. Moreover, these ZnO nano-rods were able to sense ethanol vapour, even at room temperature. This can provide a CO sensing platform with a high sensitivity and low operating temperature with very good reproducibility. Moreover, CuO thin film based low ppm CO sensor, operating at lower temperature, can significantly reduce the power consumption. In case of ethanol sensing, room temperature operation is most attractive feature as it can drastically reduce the power consumption. Finally, all sensor materials are grown through physical growth route and thermal oxidation process for sufficiently long duration, which confirms their thermodynamic stability during the sensing operation.

Bibliography

[1]   B. K. Meyer, H. Alves, D. M. Hofmann, W. Kriegseis, D. Forster, F. Bertram, J. Christen, A. Hoffmann, M. Strabburg, M. Dworzak, U. Haboeck and A. V. Rodina, Physics Status Solidi B 241 (2004) 231.

[2]   C. Jagadish and S. J. Pearton, "Zinc Oxide: Bulk, Thin Films and Nanostructures, Processing, Properties and Application", Elsevier (2006).

[3]   H. A. Wahab, A. A. Salama, A. A. El-Saeid, O. Nur, M. Willander and I. K. Battisha, Results in Physics 3 (2013) 46.

[4]   B. Cao, W. Cai and H. Zeng, Applied Physics Letters 88 (2006) 161101.

[5]   X. Wang, Y. Ding, Z. Li, J. Song and Z. Lin Wang, Journal of Physical Chemistry C 113 (2009) 1791.

[6]   A. Umar and Y. B. Hahn, Nanotechnology 17 (2006) 2174.

[7]   H. Zhang, D. Yang, Y. Ji, X. Ma, J. Xu and D. Que, Journal of Physical Chemistry B 108 (2004) 3955.

[8]   M.S. Wagh, G.H. Jain, D.R. Patil, S.A. Patil and L.A. Patil, Sensors and Actuators B 115 (2006) 128.

[9]   R. Kumar, O. Al. Dossary, G. Kumar and A. Umar, Nano-Micro Letters 7 (2015) 97.

[10]   O. Lupan, G. Chai and L. Chow, Microelectronics Engineering 85 (2008) 2220.

[11]   X. Pan and X. Zhao, Sensors 15 (2015) 8919.

[12]   T. K. kumar, R. Jayaprakash, T. Prakash, D. Sathyaraj, N. Donato, S. Licoccia, M. Latino, A. Stassi and G. Neri, Nanotechnology 22 (2011).

[13]   L. Wang, Y. Kang, X. Liu, S. Zhang, W. Huang and S. Wang, Sensors and Actuators B 162 (2012) 237.

[14]   A. Jain, R. K. Baranwal, A. Bharti, Z. Vakil and C. S. Prajapati, Sensing D 790359 (2013) 1.

[15]   Q. H. Li, Y. X. Liang, Q. Wan and T. H. Wang, Applied Physics Letters 85 (2004) 6389.

[16]   Q. Wan and T. H. Wang, Chemistry Communications 30 (2005) 3841.

[17]   Y. J. Chen, L. Nie, X. Y. Xue, Y. G. Wang and T. H. Wang, Applied Physics Letters 88 (2006) 083105.

[18]   E. Dilonardo, M. Penza, M. Alvisi, C. Di Franco, F. Palmisano, L. Torsi and N. Cioffi Beilstein J. Nanotechnol. 7 (2016) 22.

[19]   P. Zhang, G. Pan, B. Zhang, J. Zhen and Y. Sun, Materials Research 17 (2014) 817.

[20]   B. Zielinska, B. Michalkiewicz, E. Mijowska and R. J. Kalenczuk, Nanoscale Research Letters 10 (2015) 1.

[21] P. Liu, Y. Hu, X. Liu, T. Wang, P. Xi, S. Xi, D. Gao and J. Wang, Journal of Materials. Chemistry A 7 (2019) 12851.

[22] A. Tsukazaki, M. Kubota, A. Ohtomo, T. Onuma and K. Ohtani, Journal of Applied Physics 44 (2005) 20.

[23] Z. K. Tang, G. K. L. Wong, P. Yu, M. Kawasaki, A. Ohtomo, H. Koinuma and Y. Segawa, Applied Physics Letters 72 (1998) 3237.

[24] Z. Alaie, S. M. Nejad and M. H. Yousefi, Materials Science in Semiconductor Processing 29 (2015) 16.

[25] D. Basak, G. Amin, B. Mallik, G. K. Paul and S. K. Sen, Journal of Crystal Growth 256, (2003) 73.

[26] D. Lee, W. Bae, I. Park, D. Y. Yoon, S. Lee and C. Lee, Solar Energy Materials & Solar Cells 95 (2011) 365.

[27] Y. Nishi, T. Miyata and T. Minami, Thin Solid Films 528 (2013) 72.

[28] O. Caglar, P. Carroy, P. A. Losio and I. Sinicco, Solar Energy Materials & Solar Cells 144 (2016) 55.

[29] D. U. Tulyaganov, S. Agathopoulos, H. R. Fernandes and J. M. F. Ferreira, Journal of the European Ceramic Society 27 (2007) 1665.

[30] Bacaksiz, E. Parlak, M. Tomakin, M. Ozcelik, A. Karakiz and M. Altunbas, Journal of Alloys and Compounds 466 (2008) 447.

[31] S. Choudhary, J. V. N. Sarma, S. Pande, S. A. Girard, P. Turban, B. Lepine and S. Gangopadhyay, AIP Advance 8 (2018) 055114.

[32] L. D. L. S. Valladares, D. H. Salinas, A. B. Dominguez, D. A. Najarro, S. I. Khondaker, T. Mitrelias, C. H. W. Barnes, J. A. Aguiar and Y. Majima, Thin Solid Films 250 (2012) 6368.

[33] S. Choudhary and S. Gangopadhyay, AIP Conference Proceedings 1989 (2018) 020007.

[34] G.G. Rusu, Mihaela Gırtan and M. Rusu, Superlattices and Microstructures 42 (2007) 116.

[35] M. R. Khanlary, V. Vahedi and A. Reyhani, Molecules 17 (2012) 5021.

[36] K. Lim, M. A. A. Hamid, R. Shamsudin, N. H. Al-Hardan, I. Mansor and W. Chiu, Materials 9 (2016) 300.

[37] ASTM X-ray powder data file, card no. 5-0664.

[38] I. Mihailova, V. Gerbreders, E. Tamanis, E. Sledevskis, R. Viter and P. Sarajevs, Journal of Non-Crystalline Solids 377 (2013) 212.

[39] M. Reza Khanlary, V. Vahedi and A. Reyhani, Molecules 17, 5021-5029 (2012).

[40] K. U. Isah, A. M. Ramalan, U. Ahmadu, S. O. Ibrahim, J. A. Yabagi and B. J. Jolayemi, Asian Journal of Applied Sciences 9 (2016) 159.

[41] A. Umar and Y. B. Hahn, Nanotechnology 17 (2006) 2174.

[42] Z. L. Wang, Applied Physics A: Material Science Process. 88 (2007) 7.

[43]   X. G. Han, H. Z. He, Q. Kuang, X. Zhou, X. H. Zhang, T. Xu, Z. X. Xie, and L. S. Zheng, Journal of Physics and Chemistry C 113 (2009) 584.

[44]   X. Cai, B. Han, S. Deng, Y. Wang, C. Dong, Y. Wang and I. Djerdj, CrystEngComm 16 (2014) 7761.

[45]   S. Ho Na and C. Hong Park, Journal of the Korean Physical Society 54 (2009) 867.

[46]   P. Shankar and J. B. B. Rayappan, RSC Advance 5 (2015) 85363.

[47]   S.Guillemin, L. Rapenne, H. Roussel, E. Sarigiannidou, G. Bremond, and V. Consonni, Journal of Physics and Chemistry C 117 (2013) 20738A. Umar and Y. B. Hahn, Nanotechnology 17 (2016) 2174.

[48]   S. Baskoutas, P. Giabouranis, S. N. Yannopoulos, V. Dracopoulos, L. Toth, A. Chrissanthopoulos and N. Bouropoulos, Thin Solid Films 515 (2007) 8461.

[49]   John F. Moulder, William F. Stickle, Peter E. Sobol and Kennetlf D. Bomben, "Handbook of X-ray Photoelectron Spectroscopy", Perkin-Elmer Corporation, W Physical Electronics Division (1993) 000833.

[50]   A. Sahai and N. Goswami, AIP Conference Proceedings 1665 (2015) 050023.

[51]   K.G. Saw, K. Ibrahim, Y.T. Lim and M.K. Chai, Thin Solid Films 515 (2007) 2879.

[52]   R. Al-Gaashani, S. Radiman, A. R. Daud and N. Tabet, Ceramics International 39 (2013) 2283.

[53]   A. Moezzi, A. M. McDonagh and M. B. Cortie, *Chemical Engineering Journal* 185-186 (2012) 1.

[54]   N. S. Kumar, K. V. Bangera and G. K. Shivakumar, Applied Nanoscience 4 (2014) 209.

[55]   N. Bouhssira, S. Abed, E. Tomasella, J. Cellier, A. Mosbah, M. S. Aida and M. Jacquet, Applied Surface Seience 250 (2006) 5594.

[56]   Y. I. Alivov, A. V. Chernykh, M. V. Chukichev and R. Y. Korotkov, Thin Solid Films 473 (2005) 241.

[57]   L. S. Mende and J. L. M. M. Driscoll, Materials today 10 (2007) 40.

[58]   V.A. Nikitenko, Journal of Applied Spectroscopy 57 (1993) 783.

[59]   D. C. Look, J. W. Hemsky and J. R. Sizelove, Physical Review Letter 82 (1998) 2552.

[60]   J.W. Orton and M.J. Powell, Reports on Progress in Physics 43 (1980) 81.

[61]   D. E. Williams, Sensors Actuators B 57 (1999) 1.

[62]   A. Kolmakov, Y. Zhang, G. Cheng and M. Moskovits, Advanced Materials 15 (2003) 997.

[63]   M. Takata, D. Tsubone and H. Yanagida, Journal of American Ceramic Socity 59 (1976) 4.

[64]   G. Sberveglieri, "Gas Sensors: Principle, Operation and Developments", Springer Secience & Business Media (2012), 409.

[65]   C. C. Hsiao and L. S. Luo, Sensors 14 (2014) 12219.

[66]   S. J. Chang, T. J. Hsueh, I. C. Chenand and B. R. Huang, Nanotechnology 19 (2008) 175502.

[67]   P. S. Shewale, Y. S. Yu, J. H. Kim, C. R. Bobade and M. D. Uplane, Journal of Analytical and Applied Pyrolysis 112 (2015) 348.

[68]   J. Wang, J. Yang, N. Han, X. Zhou, S. Gong, J. Yang, P. Hu and Y. Chen, Materials and Desigen 121 (2017) 69.